nature nanotechnology

ARTICLES

https://doi.org/10.1038/s41565-021-01010-2

Check for updates

Light-activated interlayer contraction in two-dimensional perovskites for high-efficiency solar cells

Wenbin Li[1,2], Siraj Sidhik[1,3], Boubacar Traore[3,4], Reza Asadpour[5], Jin Hou[6], Hao Zhang[1,2], Austin Fehr[1], Joseph Essman[1], Yafei Wang[1], Justin M. Hoffman[7], Ioannis Spanopoulos[7], Jared J. Crochet[8], Esther Tsai[9], Joseph Strzalka[10], Claudine Katan[4], Muhammad A. Alam[5], Mercouri G. Kanatzidis[7], Jacky Even[5], Jean-Christophe Blancon[1]✉ and Aditya D. Mohite[1,2]✉

Understanding and tailoring the physical behaviour of halide perovskites under practical environments is critical for designing efficient and durable optoelectronic devices. Here, we report that continuous light illumination leads to >1% contraction in the out-of-plane direction in two-dimensional hybrid perovskites, which is reversible and strongly dependent on the specific superlattice packing. X-ray photoelectron spectroscopy measurements show that constant light illumination results in the accumulation of positive charges in the terminal iodine atoms, thereby enhancing the bonding character of inter-slab I–I interactions across the organic barrier and activating out-of-plane contraction. Correlated charge transport, structural and photovoltaic measurements confirm that the onset of the light-induced contraction is synchronized to a threefold increase in carrier mobility and conductivity, which is consistent with an increase in the electronic band dispersion predicted by first-principles calculations. Flux-dependent space-charge-limited current measurement reveals that light-induced interlayer contraction activates interlayer charge transport. The enhanced charge transport boosts the photovoltaic efficiency of two-dimensional perovskite solar cells up to 18.3% by increasing the device's fill factor and open-circuit voltage.

Two-dimensional (2D) hybrid perovskites have recently emerged as solution-processed semiconductors with unique physical properties that offer opportunities for optoelectronics, spintronics and energy-conversion technologies of the future[1–5]. Most of the reported structures are formed by the chemical assembly of stacks of nanometre-thick hybrid perovskite layers, separated by bulky insulating organic spacer cations such as alkylammonium or thienyl-, phenyl- and cyclohexyl-based monovalent cations and adopt a so-called Ruddlesden–Popper (RP) phase[6–8]. The composition of the organic moieties and the perovskite layer thickness (expressed by the n value in the chemical formula $L_2A_{n-1}B_nX_{3n+1}$ where L is the organic monovalent spacer; A is methylammonium (MA), formamidinium (FA) or Cs; B is a divalent metal such as Pb or Sn; and X is a halide: I, Br or Cl) define the crystal phase, structural, mechanical, electronic and optical properties of resulting 2D perovskites[8–17].

Recent work by Kanatzidis and coworkers demonstrated that using spacer dications, such as piperidinium (4AMP) or a mixture of small cations such as guanidinium (GA) and MA instead of the well-known butylammonium (BA), leads to the formation of 2D hybrid perovskites with different crystal structures such as Dion–Jacobson (DJ) and alternating cation interlayer (ACI), in which the interlayer distance is much smaller than in the well-studied RP[7,8,18,19]. For iodine perovskites, which are the most suitable for single-junction solar cells, the I–I distance can be as small as 4 Å compared to 7 Å with BA. Moreover, the stacking of the perovskite layers and the use of the short cation (4AMP) in the DJ structure impose a perfectly eclipsed alignment on the layer stacking, resulting in weak but notable electronic coupling between the iodine atoms directly facing each other across the organic interlayer[18,19]. Due to the recombination of carriers at the organic–inorganic interfaces and imperfect crystal packing in thin films, the 2D hybrid perovskites exhibit inferior charge transport properties as compared to their three-dimensional (3D) counterparts, which has a direct impact on the efficiency of photovoltaic devices[12,20,21]. Tailoring interlayer interactions by using suitable organic cations or external mechanical stress has been predicted to enhance the electronic coupling between perovskite layers across the organic spacer and significantly enhance the charge transport in 2D hybrid perovskites[9,22–27]. This approach would enable the synthesis of thicker films (>400 nm, more like 3D films), increase the absorption and bridge the efficiency gap between the 2D and 3D perovskites[20].

Here, we show that continuous illumination of DJ and ACI 2D hybrid perovskites results in a lattice contraction with a 0.4% decrease in the lattice parameter of the perovskite layer plane (in-plane) direction and >1% decrease in the lattice parameter of

[1]Department of Chemical and Biomolecular Engineering, Rice University, Houston, TX, USA. [2]Applied Physics Program, Smalley-Curl Institute, Rice University, Houston, TX, USA. [3]Institut FOTON, University Rennes, INSA Rennes, CNRS, Rennes, France. [4]Univ Rennes, ENSCR, INSA Rennes, CNRS, ISCR (Institut des Sciences Chimiques de Rennes) -UMR 6226, Rennes, France. [5]School of Electrical and Computer Engineering, Purdue University, West Lafayette, IN, USA. [6]Department of Materials Science and NanoEngineering, Rice University, Houston, TX, USA. [7]Department of Chemistry, Department of Materials Science and Engineering, Northwestern University, Evanston, IL, USA. [8]Los Alamos National Laboratory, Los Alamos, NM, USA. [9]Center for Functional Nanomaterials, Brookhaven National Laboratory, Brookhaven, NY, USA. [10]X-Ray Science Division, Argonne National Laboratory, Argonne, IL, USA. ✉e-mail: blanconjc@gmail.com; adm4@rice.edu

the out-of-plane direction. In-situ X-ray photoelectron spectroscopy (XPS) measurements performed on single crystals and thin films under continuous illumination reveal that upon illumination, the iodide ions become electron poor (more positively charged or oxidized), which triggers an enhancement of the I–I interactions across an organic barrier. This decreases the effective interlayer distance and results in a threefold, step-like increase in the charge carrier mobility. Importantly, the abrupt change in the mobility is perfectly in sync with the onset of lattice contraction in the in-situ device grazing incident wide-angle X-ray scattering (GIWAXS). Furthermore, light-intensity-dependent GIWAXS and mobility measurements elucidate a percolation-based mechanism, which explains the threefold increase in mobility and the observed timescale of the light-induced changes and the subsequent relaxation. Theoretical calculations reveal that the localization of holes on the iodine atoms results in larger electronic dispersion along the stacking axis, which is consistent with our experimental observation of enhanced charge transport. The improved charge transport results in a large increase in the efficiency of a DJ-based photovoltaic device from 15.6% to 18.3%, mainly due to improved charge collection, reflected as an increase in the fill factor and open-circuit voltage of the solar cell.

Structural characterization of 2D perovskite under light

The 2D perovskites were exposed to the light from a solar simulator (air mass 1.5G) while their structure was monitored using GIWAXS as a function of illumination time (Fig. 1a). Figure 1a illustrates the experimental set-up and the corresponding GIWAXS pattern of DJ 4AMP-$MA_2Pb_3I_{10}$ (DJ $n=3$) perovskite crystal powders, which shows concentric rings with constant scattering q ($Å^{-1}$) radius corresponding to the Bragg reflections of DJ $n=3$ lattice planes identified by their Miller indices (Fig. 1b, filled curve; structure of the DJ $n=3$ in Fig. 1c; and complete q range is shown in Supplementary Fig. 1). Under constant light illumination, all the diffraction peaks decrease in intensity and shift to higher q values (Fig. 1b). The light-induced increase in the q value of the diffraction is attributed to a continuous and reversible lattice contraction in all directions. The lattice contraction corresponds to a 2% reduction in the volume of the lattice unit cell after 51 minutes of illumination (Supplementary Table 1). Detailed analysis of the evolution of the diffraction peaks (results for the 300 and 011 peaks in Supplementary Fig. 2a,b) yields a monotonic decrease of the out-of-plane and in-plane lattice parameters (Fig. 1d and Supplementary Fig. 2). After 51 minutes of illumination, we observed a contraction of the lattice by 1.0% (23.12 to 22.90 Å) and 0.56% (8.847 to 8.803 Å) in the out-of-plane and in-plane directions, respectively (Fig. 1e). These relative changes in the lattice parameter values over time, which can be interpreted as the normal strain induced in the lattice by light, reveal that the light-induced lattice contraction effect is significantly stronger in the direction of the stacking axis (out-of-plane) as compared to the in-plane direction. In addition, we also observed an increase in the intensity of the diffraction peaks stemming from a new polymorph of the DJ $n=3$ (labelled 'P' in Supplementary Fig. 2a,b), which exhibits a first-order contraction of the lattice volume by about 7.0% as compared to the nominal DJ $n=3$ phase before illumination. However, we emphasize that the latter effect was observed only on powder samples and absent in DJ $n=3$ single crystals (Fig. 1f) or thin films integrated into solar cells (Fig. 5). These results imply that sample preparation and morphology, as well as edges and surfaces might play an important role in the manifestation of the contracted polymorph. By contrast, the continuous and reversible light-induced lattice contraction of the original perovskite phase is an intrinsic phenomenon observed for all types of samples and is a bulk property.

Next, to verify that the light-activated contraction phenomenon reported in Fig. 1 is purely light induced, we performed the following analysis. First, we confirmed that our samples did not exhibit any light-induced irreversible degradation, as the total intensity of the GIWAXS patterns remained constant during light illumination (Supplementary Fig. 2c) and the light-induced changes are reversible after placing the 2D perovskites in the dark for several hours (Fig. 1b and Supplementary Fig. 2a,b). Second, we excluded the possibility that the observed lattice contractions were due to heating by investigating the structural changes in DJ $n=3$ as a function of temperature in the dark. The temperature dependence as illustrated in Fig. 1g (and Supplementary Fig. 3a–d) showed that the diffraction peaks shift to smaller q values with increasing temperature, which is a clear indication of a lattice expansion and is opposite to the light-induced results reported in Fig. 1b,d. In addition, above −40 °C, we observed the coexistence of the original phase and the new polymorph all the way up to 80 °C (Supplementary Fig. 3a,b). We note that coexistence between polymorphs, including phases with the same space groups, has been observed in 2D perovskites, and recent studies suggest that their transformation can be tuned by temperature and pressure[9,24,25].

To understand how the light-induced structural changes observed in DJ $n=3$ depend on its specific crystal structure, we investigated two other types of 2D perovskite structures (Fig. 2a): ACI perovskites ($GAMA_3Pb_3I_{10}$, $n=3$ and $GAMA_2Pb_2I_7$, $n=2$; Supplementary Fig. 4) and RP perovskites ($BA_2MA_3Pb_3I_{10}$, $n=3$; Supplementary Fig. 5)[7,19]. We observed that both the ACI $n=2$ and $n=3$ showed light-induced structural changes similar to the DJ $n=3$. Surprisingly, the RP $n=3$ exhibited no measurable structural changes after one hour of illumination. Figure 2b presents a quantitative comparison of both the in-plane and out-of-plane light-induced normal strain for all the 2D perovskite samples (also summarized in Supplementary Table 1). The in-plane compressive strain showed a similar trend in both the DJ and ACI samples and reached values between −0.4% and −0.5%, respectively, after 51 minutes of illumination. On the other hand, the out-of-plane strain amplitude increased at a much faster rate under continuous illumination and reached values between −0.6% and −1.0%, with DJ $n=3$ exhibiting the largest compressive strain and ACI $n=3$ the smallest one. We note that while the light did not induce any structural changes in the RP $n=3$, we observed a lattice expansion upon heating in the RP samples in the dark (Supplementary Fig. 3), which further confirmed that light-induced temperature effects can be ignored in our in-situ GIWAXS experiments. Finally, similar to the DJ $n=3$, both the ACI and RP 2D perovskites exhibited an increase in the polymorphic phase as a function of increasing temperature (Supplementary Fig. 4e,h,i). Nevertheless, these measurements suggest that a correlation exists between the different structural phases of 2D perovskite and the effect of light-induced contraction.

Mechanism of light-activated interlayer contraction

To understand the mechanistic origin of the light-induced lattice contraction, we performed XPS measurements before and after light exposure on millimetre-sized DJ and RP single crystals (Fig. 2c,d). This allowed us to directly probe the chemical bonding states of the Pb 4*f* and I 3*d* electron core levels (Fig. 2c,d, left and right, respectively). Our results showed a clear blue shift in the binding energies of both iodine and lead atoms in the DJ sample. The blue shift in the bonding states indicates the loss of electrons (or oxidation) of the iodide ion. The more positively charged iodides across the interlayer can undergo an oxidative coupling, which results in the out-of-plane contraction and a decrease in the effective interlayer distance. We note that this mechanism is akin to the well-known formation of polyiodides, specifically oxidative coupling of iodide ions to create I_n^- molecular weakly bound polyiodide oligomers[28]. A similar shift was also observed for Pb core levels; however, the shift in energy for the iodide core levels was larger (0.25 ± 0.002 eV versus 0.20 ± 0.006 eV, iodide versus lead, respectively). This is

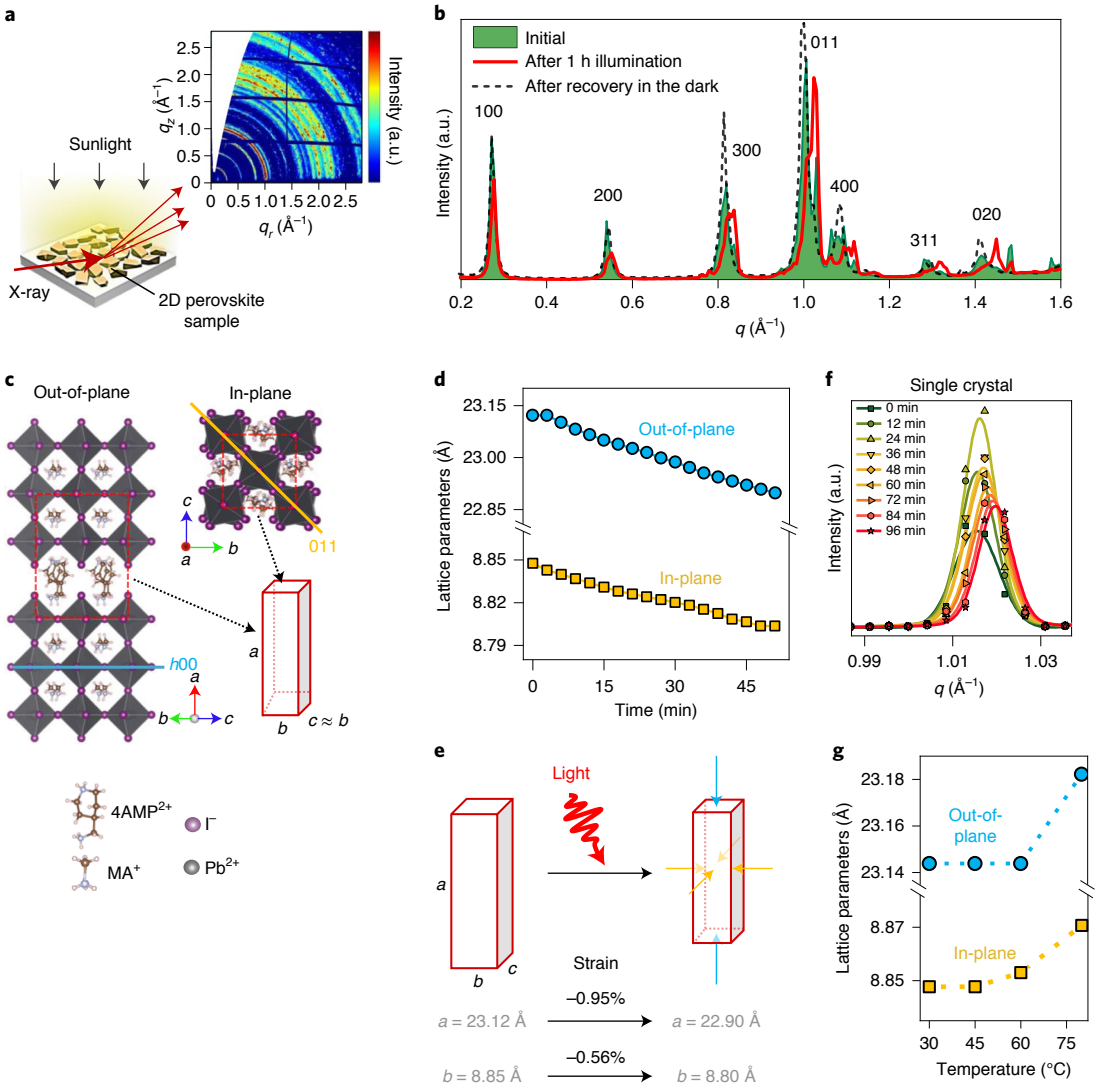

Fig. 1 | Evolution of the structure of the DJ $n = 3$ perovskites under continuous light illumination. a, Schematic of the in-situ GIWAXS experiment and crystal-powder diffraction pattern. q_r and q_z is the planar and normal direction of the scattering vector **q**. **b**, Corresponding angular-integrated diffraction spectra before and after light illumination, and after resting the sample in the dark for a few hours. **c**, DJ $n = 3$ structure with diffraction planes and Miller indices (h is integer). The unit cell in red is defined by the lattice parameters a, b and c. **d**, Corresponding evolution of the out-of-plane (a axis) and in-plane (b axis and c axis, with $b \approx c$) lattice parameters under illumination. **e**, Overview of the light-induced lattice contraction. **f**, Diffraction spectra of DJ $n = 3$ single crystals as a function of illumination time. **g**, Evolution of the DJ $n = 3$ lattice parameters at high temperature.

consistent with the fact that electrons on the Pb bonding states are quickly delocalized and as a result experience a secondary oxidative environment[29,30]. In sharp contrast to the DJ perovskite, the RP system exhibited no measurable shift in the binding energies under light exposure (Fig. 2d). Moreover, the 3D structure resulted in a red shift in Pb and I core levels, consistent with previous reports (Supplementary Fig. 6a,b)[31] and opposite to the trend observed for 2D perovskites. These XPS trend measurements clearly imply that light-induced out-of-plane contraction is correlated to the interlayer iodide interactions in DJ and ACI 2D perovskites, in which the interlayer distance is the shortest.

Previous reports claim that the orbital nature of the valence band in the perovskites is antibonding in character and has a strong contribution from the $6s^2$ states of the Pb^{2+} atoms as well as the filled p states from iodine atoms[14,18,27]. Therefore, light excitation across the bandgap involves the creation of holes via the depopulation of antibonding states with both Pb and I contributions in the valence band. Because of the proximity of the adjacent slabs enabled by the very short spacer cations, some holes can get trapped through the enhanced I–I weakly bonding interactions across the slabs, resulting in contraction along the out-of-plane direction. Moreover, a key requirement for this mechanism to be activated is that the I–I distance across the slabs must be short; therefore, this effect of light-activated interlayer contraction is observed only in DJ and ACI perovskites.

To gain a deeper insight into the mechanism proposed by the in-situ XPS measurements and to understand the impact of the out-of-plane light-induced contraction on the band structure, we performed first-principles calculations based on density functional theory (DFT) for 2D perovskites under various charged states (modelling details in Methods). Our model confirmed that the lattice contraction stems from the accumulation of photo-generated holes in the bulk, which leads to a compressive strain of the perovskite superlattice through a decrease of the interlayer spacing (Fig. 3b and Supplementary Fig. 6c,d). DFT calculation also predicts that the light-induced effects are more prominent in the DJ versus ACI,

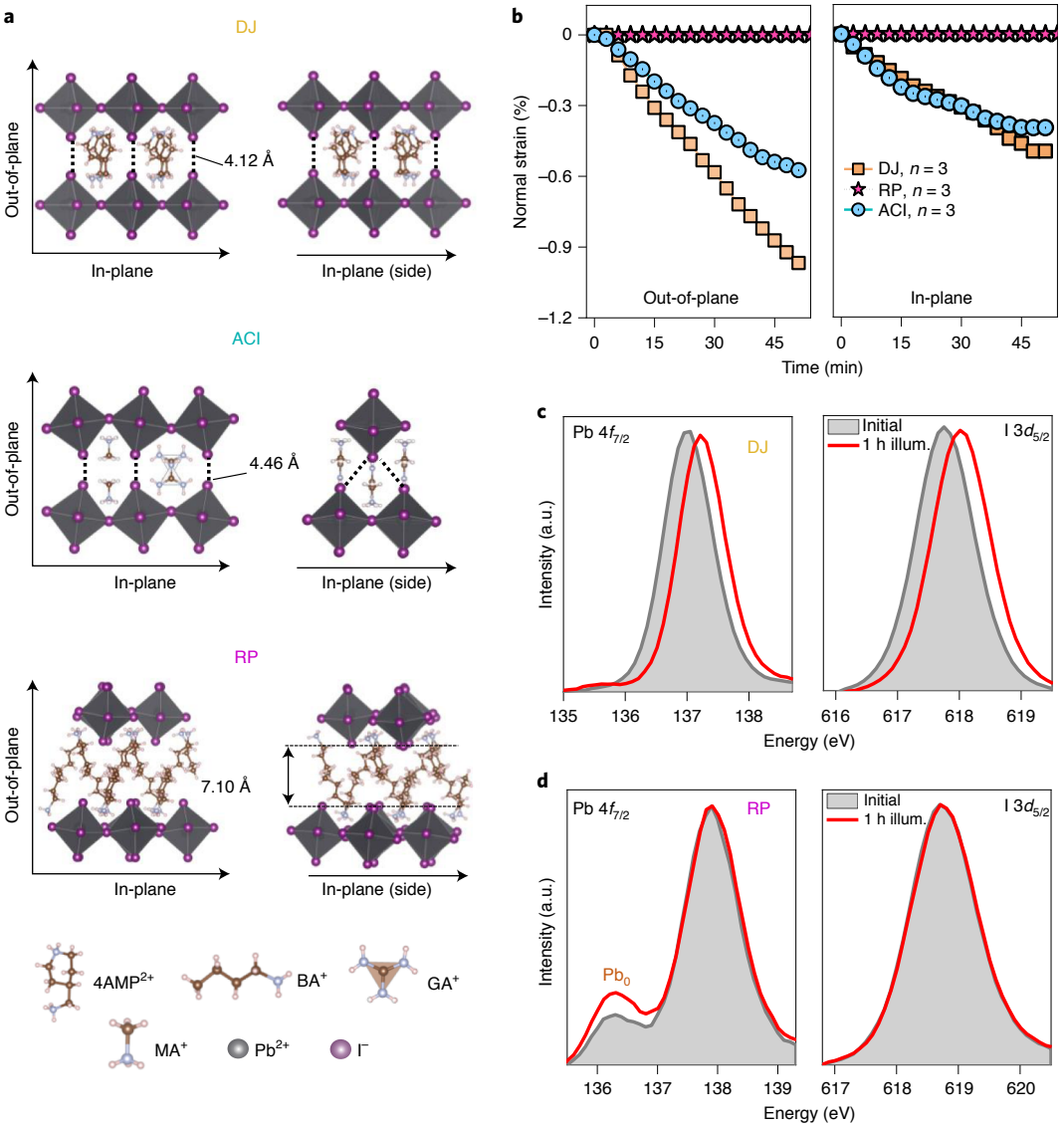

Fig. 2 | Mechanistic origin of the light-induced contraction. a, Structure of the three types of 2D perovskites with different superlattice packing and different types of organic spacer cations, with different interlayer spacing lengths. The dashed lines in the DJ and ACI structures indicate weak I···I interaction through the interlayer space, which is absent in the RP case. **b**, Evolution of the normal strain for the out-of-plane and in-plane Bragg peaks under continuous sunlight illumination for DJ $n=3$, ACI $n=3$ and RP $n=3$. We define the normal strain induced by light as the relative changes in the q value, $1-q(t)/q(t_0)$, where t_0 is a time of zero and t is the light illumination time. **c**,**d**, Before and after light-illuminated (illum.) XPS spectra of DJ $n=3$ (**c**) and RP $n=3$ (**d**) perovskite. The left-hand plot is the lead 4f core level and the right-hand plot is the iodide 3d core level. In the RP spectra, metallic lead is observed and is marked by Pb_0.

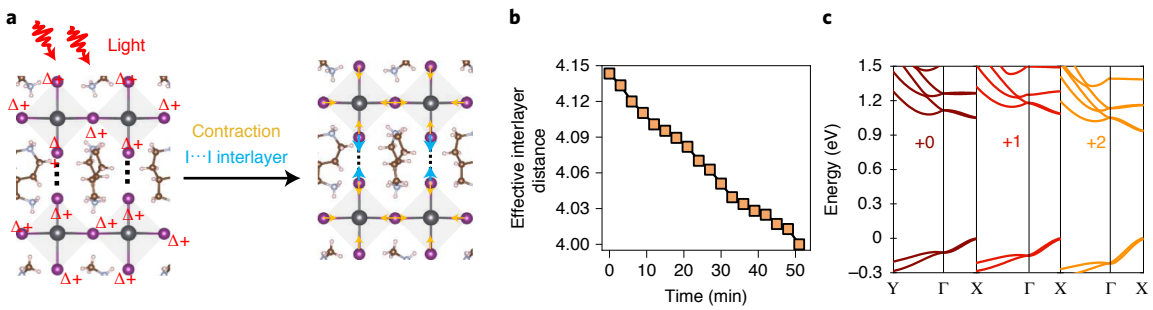

Fig. 3 | Interlayer distance and band structure. a, Schematic describing the origin of the light-induced lattice contraction in 2D perovskites. The model shows that the photoexcited holes located on the I atoms (Δ+ signs on the left panel) drive the interlayer contraction through the reduction of the I···I distance between iodine atoms that are across the organic spacer cations. **b**, Evolution of the shortening in the effective interlayer distance under constant illumination. **c**, DFT calculation of the band structure of DJ $n=3$ as a function of positive charge carrier (hole) injection.

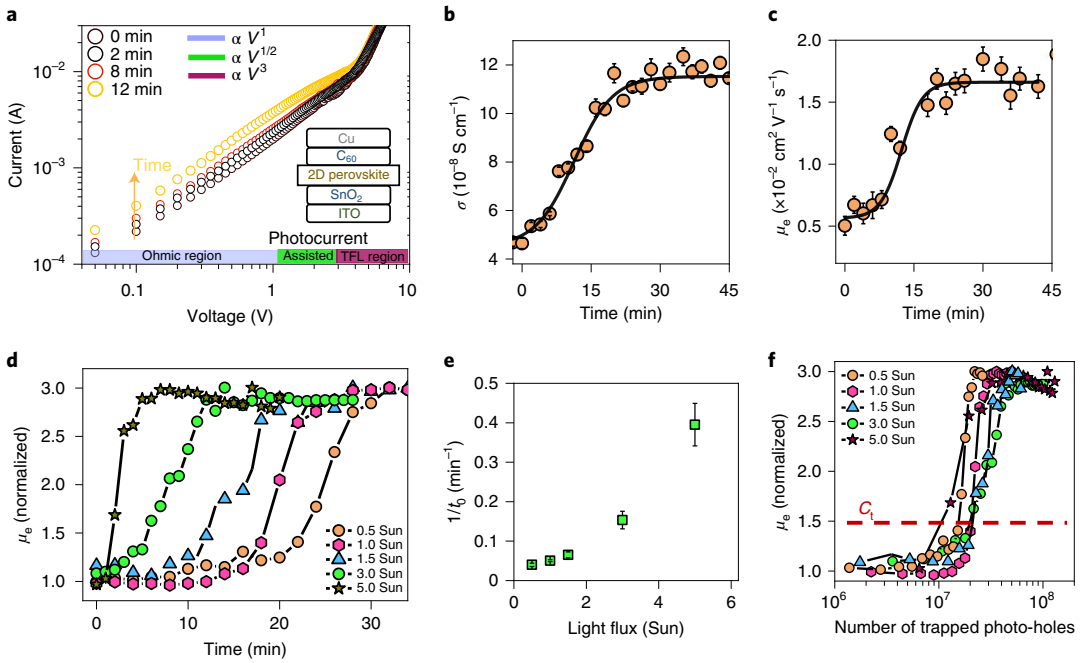

Fig. 4 | Electron mobility as a function of light illumination. a, Evolution of the current–voltage trace for an electron-only device as a function of light illumination time at 1 Sun intensity. Three regions are indicated on the plot: ohmic, space-charge-limited photocurrent and TFL. Device schematic is shown as the inset. **b**,**c**, Corresponding changes in the conductivity (σ; **b**) and in the electron mobility (μ_e; **c**) as a function of light illumination. Error bars are shown for each point and are represented by the 5% fitting error. **d**, Light-intensity-dependent (in units of number of Suns) electron mobility SCLC measurements. **e**, Corresponding relationship between inverse t_0, percolation threshold time and incident light intensity. Error bars are shown for each point and are represented by sampling time error. **f**, Electron mobility as a function of trapped photo-holes under different light intensities. The red line denotes the percolation threshold (C_t) for the photo-generated hole carriers.

which confirms the fact that iodide interactions are stronger in the DJ perovskite with its shorter interlayer iodide distance (4.12 Å) compared to the ACI perovskite (4.46 Å; Supplementary Tables 3 and 5). Furthermore, to mimic the enhancement of the inter-slab I–I bonds by the accumulation of holes on the iodides, we calculated the electronic band structure of the DJ perovskite as a function of positive charge carrier (hole) injection (Fig. 3c). Our simulation shows that after one- to two-hole injections, the curvature at the valance band maxima and conduction band minima exhibited a larger dispersion along the octahedra stacking axis (Γ–X) compared to the neutral case. This dispersion implies that a notable change in the charge carrier properties can be expected. Finally, we note that a positively charged RP perovskite is predicted to undergo a vertical lattice contraction according to DFT calculations, therefore confirming that the absence of lattice contraction and XPS shifts (Fig. 2b,d) is attributed to the lack of positive charge accumulation in the case of RP-phase 2D perovskites. This is reasonable because such accumulation requires the existence of short I–I in the structure to begin with. In fact, two pathways that can efficiently drive away the photo-generated charge carriers in the bulk of RP perovskites are via low-energy states at their edge surfaces, or by the quick formation of Wannier excitons[32–34].

In-situ transport and device measurements

Motivated by the DFT band-structure calculations, which predict an increase in band dispersion upon light-induced contraction in the out-of-plane direction, the next logical step was to quantify the impact of contraction on the electronic transport properties. We conducted in-situ space-charge-limited current (SCLC) measurements under continuous light illumination (Fig. 4a) by fabricating an electron-only device by sandwiching a DJ $n=3$ 2D perovskite thin film between indium tin oxide (ITO)/SnO_2 and C_{60}/Cu (fabrication process in the Methods). We first measured the current–voltage (J–V) characteristics of the device in the dark and observed two regimes (Supplementary Fig. 7a). At low voltages, the J–V curve showed a linear dependence ($J=\alpha V$) indicating an ohmic response. At higher voltages (>3 V), the linear response shifted towards a nonlinear regime ($J=\alpha V^3$) signalling a transition to a trap-filled limited (TFL) region (details of the fitting are in the Methods). These results agree well with previous reports[21,35,36]. Next, we exposed the device to constant 1 Sun light illumination. A new sublinear response ($J=\alpha V^{1/2}$) was observed in the J–V curve between the ohmic and TFL regions (Fig. 4a and Supplementary Fig 7b). We attribute this to the space-charge-limited photocurrent regime, where generated photocarrier and injected free carrier concentrations exceed the background charge carrier concentration and accumulate at one of the interfaces to create a space-charge build-up[37,38]. Nevertheless, we directly monitored the J–V trace of the electron device under light illumination, which is shown in Fig. 4a. We observed a sudden jump in the J–V trace upon 10 minutes of light illumination. The conductivity analysis (extracted from the fit in the ohmic region) indicates that after 10 minutes of light illumination, a sigmoidal increase of conductivity occurred, from 50×10^{-9} S cm^{-1} to 120×10^{-9} S cm^{-1} (Fig. 4b). Similarly, the carrier mobility increased from 0.5×10^{-2} cm^2 V^{-1} s^{-1} to 1.5×10^{-2} cm^2 V^{-1} s^{-1} after 10 minutes of light soaking (Fig. 4c). These results suggest that the charge transport is significantly enhanced within the short time of 10 minutes, even though the effect of light-induced contraction had just initiated. The improvement in the charge transport properties is consistent with the increase in the out-of-plane dispersion predicted by DFT simulations and indicates the activation of the interlayer transport pathway. In fact, recent work by Ma et al. has shown that when reducing the length of the organic spacer cation, a new interlayer transport channel is created[39].

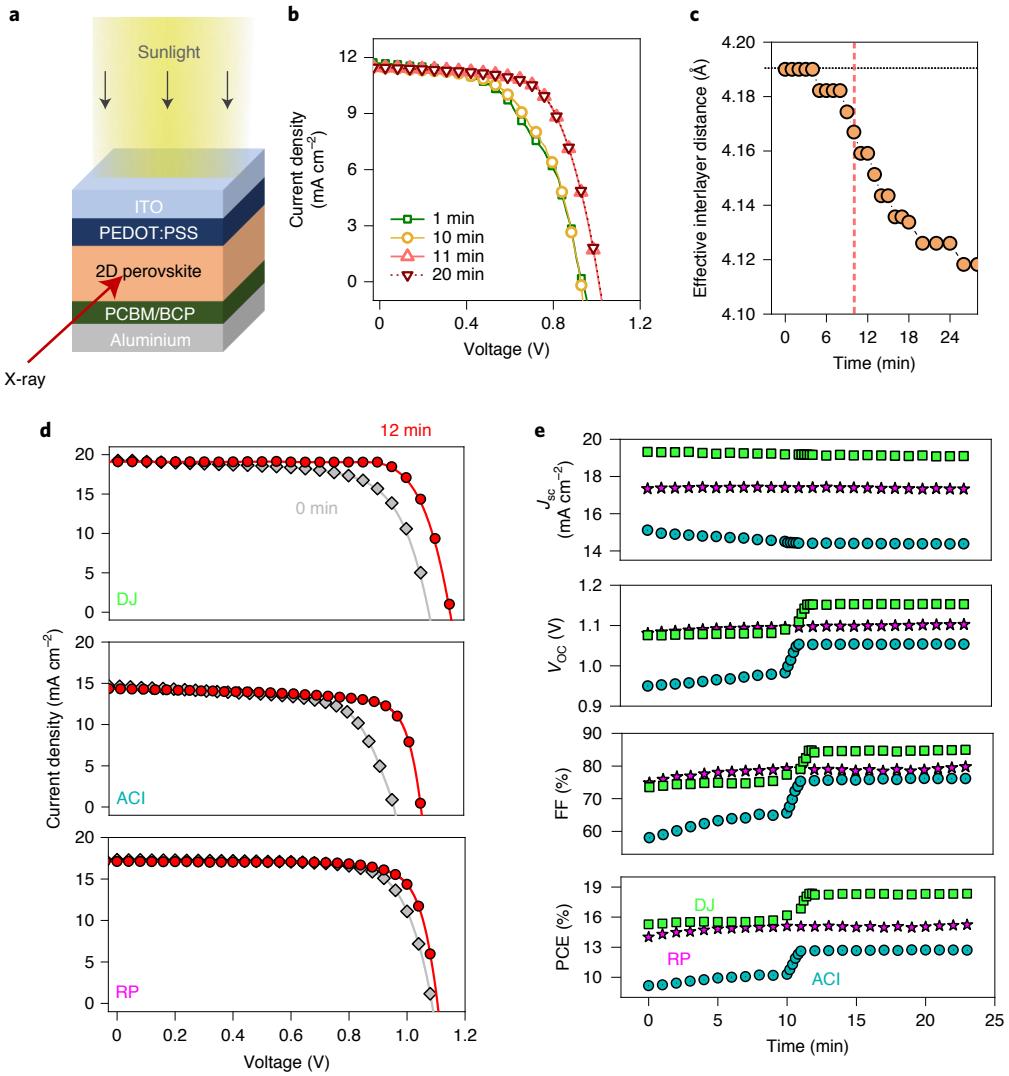

Fig. 5 | Effects of continuous light illumination on the performance of 2D perovskite solar cells. a, Device architecture used for fabricating solar cells. PCBM/BCP, [6,6]-phenyl-C_{61}-butyric acid methyl ester/bathocuproine; PEDOT:PSS, poly(3,4-ethylenedioxythiophene) polystyrene sulfonate. **b**, Evolution of the current–voltage characteristics of the solar cell under constant AM 1.5 one Sun intensity illumination measured in the DJ device during in-situ GIWAXS diffraction. **c**, Corresponding structural changes. The vertical dashed line indicates the time at which the solar cell performances increase drastically. The horizontal dashed line indicates the interlayer distance before light illumination. **d**, Current–voltage characteristics before and after 10 minutes of illumination with sunlight for three types of 2D perovskite solar cells using the DJ, ACI and RP 2D perovskite phases. **e**, Corresponding evolution of the solar cell figures of merit as a function of illumination time. PCE, power conversion efficiency.

To gain deeper insight into the correlation between the light-induced contraction and the enhancement in charge transport, we performed light-intensity-dependent GIWAXS and SCLC measurements, described below. GIWAXS measurements were performed on DJ $n=3$ powders using two illumination intensities, 0.4 and 1.0 Sun (Supplementary Fig. 8a). Similar to the 1 Sun measurements shown in Fig. 1, lower-light-intensity illumination induces an anisotropic contraction for the out-of-plane and in-plane diffraction planes. However, we find that at 0.4 Sun, the magnitude of the strain was lower in both directions with −0.2% compressive strain in the out-of-plane direction and −0.1% strain in the in-plane direction. Moreover, the slope of the light-induced strain for both the directions was smaller than the 1 Sun case. Next, to build on our intensity-dependent GIWAXS results, we performed a flux-dependent SCLC measurement on an electron-only device. Our SCLC results reveal several interesting phenomena: (1) a sudden sigmoidal variation (a constant lower and upper limit) of the mobility as a function of time under constant light illumination at different light intensities (Fig. 4d); (2) a threefold increase of the mobility, which is independent of the light intensity (Fig. 4d); and (3) an inverse relationship between the time of nonlinear increase and the flux of light illumination (Fig. 4e). Analogous to the classical percolation theory for electrical conductivity in an inhomogeneous medium, the transition between low and high conductive states occurs when a percolation threshold is reached due to doping[40,41]. We propose that our system follows an equivalent concept in which the method of doping is the trapping/localization of photo-generated holes at the iodine sites (threshold).

The percolation model is explained in detail in the Supplementary Discussion. In summary, our results on the intensity-dependent GIWAXS and SCLC measurements combined with a percolation model elucidate that there is a threshold number of iodine sites that need to be filled by the photo-generated holes to activate light-induced contraction and the subsequent increase in mobility (Fig. 4c). Furthermore, we performed a GIWAXS measurement on a DJ $n=3$ perovskite thin film to probe the orientation of the grains

(Supplementary Fig. 9a). The diffraction results showed that the DJ perovskite thin film exhibited a mixed orientation with mostly preferential vertical orientation (perpendicular to the substrate) and some horizontal orientation along the in-plane direction (parallel to the substrate). This indicates that before light illumination, a large fraction of the photo-generated carriers is scattered off by the organic spacer cation due to the mixed arrangements of the inorganic perovskite layers[2]. However, when the number of trapped photo-generated holes equals the percolation threshold, interlayer transport is activated by the interlayer contraction (Fig. 4f). This enhances the overall mobility and can be seen by the percolation transition in the SCLC measurement.

In order to directly probe the impact of light-induced contraction on the performance of photovoltaic devices, we performed correlated structural (GIWAXS) measurements on planar, p–i–n solar cells using DJ $n=3$ as the 2D perovskite in operando (Fig. 5a–c and Supplementary Fig. 9). Figure 5c shows the effective interlayer distance extracted from the GIWAXS measurements as a function of light illumination time. Similar to the single crystals and powder samples, thin films of DJ $n=3$ also exhibit a light-induced anisotropic compressive strain resulting in the contraction of the effective interlayer distance. Next, we observed a step-like increase in the open-circuit voltage (V_{OC}) and fill factor (FF) after 10 minutes of illumination (Fig. 5b and Supplementary Fig. 9b). The increase in these parameters is concomitant with the onset of the light-induced strain in the perovskite films indicated by the red line at 10 minutes in Fig. 5c. We also emphasize that the sudden increase in the carrier mobility described in Fig. 4c also occurs at the same time point of 10 minutes. These correlated structure, transport and device data clearly imply that the drastic improvement in the device performance is driven predominantly by the reduction of the effective interlayer distance resulting in the increase in carrier mobility, especially along the stacking direction.

Solar cell performance

Finally, to test the impact of light-induced contraction on 2D perovskite solar cells fabricated using the three types of crystal structures (DJ $n=4$, ACI $n=3$ and RP $n=4$), we monitored the evolution of their current–voltage characteristics as a function of illumination time (Fig. 5d). After 10 minutes, we observed a notable increase in the V_{OC} and FF of the DJ and ACI devices, whereas the solar cells based on RP 2D perovskite remained almost unchanged, as illustrated in Fig. 5e. The overall power conversion efficiency increased by 2.7% in solar cells based on DJ, 3.5% in ACI and less than 1.0% in RP. The overall increase in the power conversion efficiency of DJ and ACI 2D perovskite solar cells arises from a combined increase in the V_{OC} and FF. We do not observe any appreciable change in the short circuit current density J_{SC} over time, which is consistent with the invariant absorbance spectra measured as a function of light soaking. These improvements in the V_{OC} and FF are in good agreement with both the correlated in-situ solar cell and X-ray measurements described in Fig. 5a–c and the transport measurements demonstrated in Fig. 4. Moreover, solar cell measurements on 2D perovskites based on DJ, ACI and RP are consistent with the fact that light-activated contraction is observed in DJ and ACI, but not in RP 2D perovskites, as described in Fig. 2. In addition, to verify the recovery for light-induced interlayer contraction, we performed a cycle of light on and off measurements (Supplementary Fig. 10b). In agreement with the DJ powder and single-crystal results, we observed a decrease to the original solar cell efficiency after 23 minutes of resting the device in the dark. The largest increase for the champion DJ device resulted in the increase in the power conversion efficiency from 15.6% to 18.3%.

As shown in Fig. 5d,e, there are two major changes in the solar cell figures of merit after light-induced contraction: the increase of the FF and of the V_{OC}. To understand these results, we used our device drift-diffusion model, which calculated the change in the potential barrier height in the bulk by fitting the current–voltage curves before and after light soaking[20]. The simulated current–voltage characteristics before and after 10 minutes of illumination match closely with the experimental ones. Our simulations indicate that the increase in FF is due to a decrease in the potential barrier heights (Supplementary Fig. 10c–f). As shown in our previous work, the FF in 2D perovskite devices is partly governed by the recombination of the photo-generated carriers, which depends on the energy landscape of the stacked 2D quantum wells[20]. Our results indicate that the light-induced out-of-plane lattice contraction, which results from the enhanced I–I bonding across the interlayers in DJ and ACI perovskite thin films, lowers the depth of the potential barriers, thus decreasing the number of trapped carriers and thereby reducing the recombination rate. Simulations show that the change in barrier depth for DJ $n=4$ is −26.5 meV and in ACI $n=3$ is −44.5 meV (Supplementary Tables 9 and 10). Furthermore, the modelling results indicate a threefold increase in mobility after light illumination, which is in good agreement with the experimental data from the mobility measurements as illustrated in Fig. 4c.

In addition, device modelling indicates that the light-induced contraction due to an enhanced antibonding interaction modifies the ionization energy (valence band to vacuum). This leads to modification of the conduction and valence band energy profiles as validated by the blue shift of the XPS spectra on DJ perovskite films (Supplementary Fig. 6)[31]. The change in the electron affinity improves the band alignment between the electron transport layer and the 2D perovskite, thus reducing the amount of energy lost while transporting between the layers. The electron affinity of the 2D perovskite increases from 3.72 eV to 3.81 eV for DJ $n=4$ and ACI $n=3$ devices (Supplementary Table 10), thereby resulting in an increase in the V_{OC} of the solar cell. We do not observe an increase in the J_{SC} as the drift field ($V=0$ V) is sufficiently strong to extract the photo-generated carriers; therefore, the modification of the energy landscape does not change the short-circuit current.

Conclusion

These results have two key implications. First, they demonstrate that by selecting the appropriate interlayer cations and by leveraging the acute sensitivity of 2D hybrid perovskites to external stimuli, the bandgap discontinuity in the out-of-plane direction can be surmounted, and charge transport properties closer to those of 3D perovskites can be realized. Second, these results pave the path for understanding and tailoring new light–matter interactions, similar to those explored in 2D transition-metal dichalcogenides, which arise when excitations are coupled across the layered perovskite layers separated by short organic cations[42,43].

Online content

Any methods, additional references, Nature Research reporting summaries, source data, extended data, supplementary information, acknowledgements, peer review information; details of author contributions and competing interests; and statements of data and code availability are available at https://doi.org/10.1038/s41565-021-01010-2.

Received: 23 March 2021; Accepted: 13 September 2021;
Published online: 22 November 2021

References

1. Mitzi, D. B., Chondroudis, K. & Kagan, C. R. Organic-inorganic electronics. *IBM J. Res. Dev.* **45**, 29–45 (2001).
2. Tsai, H. et al. High-efficiency two-dimensional Ruddlesden–Popper perovskite solar cells. *Nature* **536**, 312–316 (2016).
3. Yuan, M. et al. Perovskite energy funnels for efficient light-emitting diodes. *Nat. Nanotechnol.* **11**, 872–877 (2016).
4. Long, G. et al. Spin control in reduced-dimensional chiral perovskites. *Nat. Photon.* **12**, 528–533 (2018).

5. Lu, H. et al. Spin-dependent charge transport through 2D chiral hybrid lead-iodide perovskites. *Sci. Adv.* **5**, eaay0571 (2019).
6. Chen, Y. et al. 2D Ruddlesden–Popper perovskites for optoelectronics. *Adv. Mater.* **30**, 1703487 (2018).
7. Cao, D. H., Stoumpos, C. C., Farha, O. K., Hupp, J. T. & Kanatzidis, M. G. 2D homologous perovskites as light-absorbing materials for solar cell applications. *J. Am. Chem. Soc.* **137**, 7843–7850 (2015).
8. Mao, L., Stoumpos, C. C. & Kanatzidis, M. G. Two-dimensional hybrid halide perovskites: principles and promises. *J. Am. Chem. Soc.* **141**, 1171–1190 (2019).
9. Billing, D. G. & Lemmerer, A. Synthesis, characterization and phase transitions of the inorganic–organic layered perovskite-type hybrids $[(C_nH_{2n+1}NH_3)_2PbI_4]$ (n = 12, 14, 16 and 18). *New J. Chem.* **32**, 1736–1746 (2008).
10. Billing, D. G. & Lemmerer, A. Synthesis and crystal structures of inorganic–organic hybrids incorporating an aromatic amine with a chiral functional group. *CrystEngComm* **8**, 686–695 (2006).
11. Mitzi, D. B. in *Progress in Inorganic Chemistry* Vol. 48 (ed. Karlin, K. D.) 1–121 (John Wiley & Sons, 1999).https://doi.org/10.1002/9780470166499.ch1
12. Tu, Q. et al. Out-of-plane mechanical properties of 2D hybrid organic–inorganic perovskites by nanoindentation. *ACS Appl. Mater. Interfaces* **10**, 22167–22173 (2018).
13. Reyes-Martinez, M. A. et al. Unraveling the elastic properties of (quasi) two-dimensional hybrid perovskites: a joint experimental and theoretical study. *ACS Appl. Mater. Interfaces* **12**, 17881–17892 (2020).
14. Katan, C., Mercier, N. & Even, J. Quantum and dielectric confinement effects in lower-dimensional hybrid perovskite semiconductors. *Chem. Rev.* **119**, 3140–3192 (2019).
15. Spanopoulos, I. et al. Uniaxial expansion of the 2D Ruddlesden–Popper perovskite family for improved environmental stability. *J. Am. Chem. Soc.* **141**, 5518–5534 (2019).
16. Gompel, W. T. M. V. et al. Towards 2D layered hybrid perovskites with enhanced functionality: introducing charge-transfer complexes via self-assembly. *Chem. Commun.* **55**, 2481–2484 (2019).
17. Ahn, J. et al. A new class of chiral semiconductors: chiral-organic-molecule-incorporating organic–inorganic hybrid perovskites. *Mater. Horiz.* **4**, 851–856 (2017).
18. Mao, L. et al. Hybrid Dion–Jacobson 2D lead iodide perovskites. *J. Am. Chem. Soc.* **140**, 3775–3783 (2018).
19. Soe, C. M. M. et al. New type of 2D perovskites with alternating cations in the interlayer space, $(C(NH_2)_3)(CH_3NH_3)_nPb_nI_{3n+1}$: structure, properties, and photovoltaic performance. *J. Am. Chem. Soc.* **139**, 16297–16309 (2017).
20. Tsai, H. et al. Design principles for electronic charge transport in solution-processed vertically stacked 2D perovskite quantum wells. *Nat. Commun.* **9**, 2130 (2018).
21. Zhang, Y., Sun, M., Zhou, N., Huang, B. & Zhou, H. Electronic tunability and mobility anisotropy of quasi-2D perovskite single crystals with varied spacer cations. *J. Phys. Chem. Lett.* **11**, 7610–7616 (2020).
22. Soe, C. M. M. et al. Structural and thermodynamic limits of layer thickness in 2D halide perovskites. *Proc. Natl Acad. Sci. USA* **116**, 58–66 (2019).
23. Leng, K. et al. Molecularly thin two-dimensional hybrid perovskites with tunable optoelectronic properties due to reversible surface relaxation. *Nat. Mater.* **17**, 908–914 (2018).
24. Liu, G. et al. Isothermal pressure-derived metastable states in 2D hybrid perovskites showing enduring bandgap narrowing. *Proc. Natl Acad. Sci. USA* **115**, 8076–8081 (2018).
25. Liu, S. et al. Manipulating efficient light emission in two-dimensional perovskite crystals by pressure-induced anisotropic deformation. *Sci. Adv.* **5**, eaav9445 (2019).
26. Yu, S. et al. Nonconfinement structure revealed in Dion–Jacobson type quasi-2D perovskite expedites interlayer charge transport. *Small* **15**, 1905081 (2019).
27. Blancon, J.-C., Even, J., Stoumpos, C. C., Kanatzidis, M. G. & Mohite, A. D. Semiconductor physics of organic–inorganic 2D halide perovskites. *Nat. Nanotechnol.* **15**, 969–985 (2020).
28. Svensson, P. H. & Kloo, L. Synthesis, structure, and bonding in polyiodide and metal iodide-iodide systems. *Chem. Rev.* **103**, 1649–1684 (2003).
29. Giovanni, D. et al. The physics of interlayer exciton delocalization in Ruddlesden–Popper lead halide perovskites. *Nano Lett.* **21**, 405–413 (2021).
30. Santomauro, F. G. et al. Localized holes and delocalized electrons in photoexcited inorganic perovskites: watching each atomic actor by picosecond X-ray absorption spectroscopy. *Struct. Dyn.* **4**, 044002 (2016).
31. Zu, F.-S. et al. Impact of white light illumination on the electronic and chemical structures of mixed halide and single crystal perovskites. *Adv. Opt. Mater.* **5**, 1700139 (2017).
32. Blancon, J.-C. et al. Extremely efficient internal exciton dissociation through edge states in layered 2D perovskites. *Science* **355**, 1288–1292 (2017).
33. Zhang, Z., Fang, W.-H., Tokina, M. V., Long, R. & Prezhdo, O. V. Rapid decoherence suppresses charge recombination in multi-layer 2D halide perovskites: time-domain ab initio analysis. *Nano Lett.* **18**, 2459–2466 (2018).
34. Neutzner, S. et al. Exciton-polaron spectral structures in two-dimensional hybrid lead-halide perovskites. *Phys. Rev. Mater.* **2**, 064605 (2018).
35. Ren, H. et al. Efficient and stable Ruddlesden–Popper perovskite solar cell with tailored interlayer molecular interaction. *Nat. Photon.* **14**, 154–163 (2020).
36. Shi, D. et al. Low trap-state density and long carrier diffusion in organolead trihalide perovskite single crystals. *Science* **347**, 519–522 (2015).
37. Goodman, A. M. & Rose, A. Double extraction of uniformly generated electron−hole pairs from insulators with noninjecting contacts. *J. Appl. Phys.* **42**, 2823–2830 (1971).
38. Mihailetchi, V. D., Wildeman, J. & Blom, P. W. M. Space-charge limited photocurrent. *Phys. Rev. Lett.* **94**, 126602 (2005).
39. Ma, C., Shen, D., Ng, T.-W., Lo, M.-F. & Lee, C.-S. 2D perovskites with short interlayer distance for high-performance solar cell application. *Adv. Mater.* **30**, 1800710 (2018).
40. Kirkpatrick, S. Percolation and conduction. *Rev. Mod. Phys.* **45**, 574–588 (1973).
41. Seager, C. H. & Pike, G. E. Percolation and conductivity: a computer study. II. *Phys. Rev. B* **10**, 1435–1446 (1974).
42. Britnell, L. et al. Strong light-matter Interactions in heterostructures of atomically thin films. *Science* **340**, 1311–1314 (2013).
43. Xia, F., Wang, H., Xiao, D., Dubey, M. & Ramasubramaniam, A. Two-dimensional material nanophotonics. *Nat. Photonics* **8**, 899–907 (2014).

Methods

Materials. The 2D perovskite precursors such as methylamine iodide (MAI), lead oxide (PbO_2), BA, 4AMP, GA hydrocholoride, anhydrous dimethyl formamide (DMF), dimethyl sulfoxide (DMSO) and hydroiodic acid (HI) were purchased from Sigma-Aldrich. MAI was purchased from Greatcell Solar. For device fabrication, ITO was from Thin Film Device, PCBM was from Sigma-Aldrich and PEDOT:PSS was from Heraeus Epurio.

Crystal and thin-film fabrication. *Powder crystal synthesis.* As previously reported in refs. [22,44], the 2D RP perovskite crystals of $BA_2MA_2Pb_3I_{10}$ were synthesized by mixing lead oxide (PbO, 99%), methylamine hydrochloride (MACl, ≥98%) and BA (99.5%) in appropriate ratios in a mixture of HI (57 wt% in H_2O) and hypophosphorous acid (H_3PO_2, 50% in H_2O). The solution was stirred at 190 °C until all the precursors were dissolved, and then allowed to cool to room temperature. This resulted in the crystallization of platelet-like powders with micrometre to millimetre sizes. The DJ perovskite crystals of 4AMP-$MA_2Pb_3I_{10}$ were prepared by combining PbO, MAI and 4AMP (96%) in appropriate ratios in a HI/H_3PO_2 solvent mixture. The solution was stirred at 240 °C until all the precursors were dissolved, and then allowed to cool to room temperature. This resulted in the crystallization of platelet-like powders with micrometre to millimetre sizes. A detailed synthesis procedure is reported in ref. [18]. The ACI perovskite crystals of $GAMA_3Pb_3I_{10}$ were prepared by combining PbO, MAI and GA hydrochloride (99%) in appropriate ratios in a HI/H_3PO_2 solvent mixture. The solution was stirred at 190 °C until all the precursors were dissolved, and then allowed to cool to room temperature. This resulted in the crystallization of platelet-like powders with micrometre to millimetre sizes. A detailed synthesis procedure is reported in ref. [19]. Finally, batches of synthesized 2D perovskite crystals were characterized using one-dimensional X-ray diffraction (Rigaku D/Max Ultima II) to determine their initial phase purity and crystal quality. Different *n*-value thicknesses of the 2D perovskites were obtained by altering the stoichiometry of the reactants in the RP, DJ and ACI perovskites, as reported in refs. [1,3,4].

Film fabrication. To produce 2D perovskite thin films for solar cell devices, we first dissolved the synthesized parent-crystal powders in a solvent with different additives. The $BA_2MA_3Pb_4I_{13}$ or $GAMA_3Pb_3I_{10}$ solution was obtained by dissolving 0.4 g of the parent crystals and 0.02 g of dried MACl in 1 ml of anhydrous DMF. The 4AMP-$MA_3Pb_4I_{13}$ solution was prepared by dissolving 0.4 g of the parent crystals in 1 ml of anhydrous DMF/DMSO (1:1) with 1 µl of HI. The prepared solution was left on the hotplate at 70 °C for 6 hours. After cooling, 100 µl of the prepared solution was instantly dropped and spin coated over substrates at 4,000 r.p.m. for 30 seconds followed by annealing at 100 °C for 10 minutes, resulting in the formation of the 2D perovskite thin films.

Large-area single-crystal synthesis. The DJ $n=3$ 4AMP-$MA_2Pb_3I_{10}$ single crystal was synthesized using PbO (Sigma-Aldrich, >99%), 4AMP (>96%) and MAI (>99.9%); HI (57.0 wt% in H_2O); and H_3PO_2 (50 wt% in H_2O). The PbO, 4AMP and MAI were mixed in the appropriate ratio in a HI/H_3PO_2 solution, indicated in ref. [18] and stirred at 240 °C until dissolved. The solution was then diluted with three times the amount of HI. Afterward, 10 µl of the diluted solution was dropped onto the glass surface and sandwiched by another piece of glass. This system was then annealed for 8 hours at 60 °C resulting in large millimetre-sized perovskite single crystal. Further details can be found in ref. [45]. The glass substrates used in this procedure were washed in water, acetone, acetone/ethanol (50:50) and isopropyl alcohol by ultrasonication for 15 min each.

Solar-cell device fabrication. We used an inverted planar device architecture with ITO/hole-transport-layer/2D-perovskite-film/electron-transport-layer/aluminium for the solar cells, as depicted in Fig. 3. This solar cell architecture used PEDOT:PSS (Heraeus Epurio, Clevios) as the hole transport layer and PCBM (Sigma-Aldrich, 99.9%) as the electron transport layer. Film fabrication steps are shown below. We first washed the patterned ITO in water, acetone, acetone/ethanol (50:50) and isopropyl alcohol by ultrasonication for 15 min each. The substrate was further dried under argon airflow and treated with UV light for 30 min. A PEDOT:PSS layer was spin coated on the clean ITO substrate at 5,000 r.p.m. for 30 seconds followed by annealing at 150 °C for 30 min to obtain a layer thickness of about 30 nm. The ITO/PEDOT:PSS substrates were subsequently transferred to an argon-filled glove box. Using the methodology from the film fabrication in the previous section, we fabricated 2D perovskite thin films of approximately 250 nm thickness on top of the ITO/PEDOT:PSS substrate. To prepare the electron transport layer, we dissolved 25 mg PCBM in 1 ml of chlorobenzene and stirred overnight at 60 °C. Afterwards, 50 µl of the PCBM solution was dropped on the ITO/PEDOT:PSS/2D-perovskite sample and spin coated at 1,000 r.p.m. for 45 seconds to form a 30 nm electron transport layer thin film. The solar cell device was completed by evaporating a 100 nm layer of aluminium using a shadow mask, yielding eight cells of 31.4 mm^2 per 25.4 × 25.4 (mm^2) area of the sample device.

Solar-cell device characterization. The performances of the fabricated solar cells were characterized by measuring the current–voltage (*J*–*V*) curves of each device illuminated by an ABB Solar Simulator from Newport (model 94011). The arc simulator modelled AM 1.5G irradiance of 100 mW cm^{-2} and was calibrated using a solar cell certified by the National Institute of Standards and Technology (NIST; Newport 91150V, International Organization for Standardization (ISO) 17025). The current was measured with a Keithley 2401 instrument at different voltage scan rates.

GIWAXS. *In-situ GIWAXS measurements.* All diffraction spectra used in this paper were high-resolution synchrotron GIWAXS patterns measured at two beamlines: 8-ID-E at the Advanced Photon Source (APS) and 11-BM at the National Synchrotron Light Source II (NSLS-II). At beamline 8-ID-E, samples were placed on a Linkam grazing incidence X-ray scattering (GIXS) stage (temperature controlled at 25 °C) inside a vacuum chamber (10^{-4} torr) with the sample 228 mm away from a Pilatus 1M (Dectris) area detector. The photon energy was 10.91 keV, and the beam size was 200 µm × 20 µm (Height × Vertical). At beamline 11-BM, two different staging schematics were used for GIWAXS measurements: (1) a built-in-lab GIXS chamber (which circulated high-purity helium gas) with the sample 257 mm away from a Pilatus 300M (Dectris) area detector and (2) a robotic stage inside a vacuum chamber (10^{-2} torr) with the sample 267 mm away from a Pilatus 800K (Dectris) area detector. The photon energy was 13.5 keV, and the beam size was 200 µm × 50 µm (Height × Vertical).

For the in-situ light-illuminated crystal GIWAXS measurements, we installed a Newport Class ABB Solar Simulator on top of each beamline chamber (schematic (1) staging chamber for beamline 11-BM) and illuminated with 1 Sun (AM 1.5G) irradiance. To calibrate the solar simulator illumination irradiance for all in-situ GIWAXS measurements, we measured 100 mW cm^{-2} using a NIST-certified Si solar cell (Newport 91150V, ISO 17025). After each powder light illumination experiment, samples were directly transferred to a vacuum chamber (10^{-2} to 10^{-4} torr) for relaxation. All in-situ light-illumination GIWAXS patterns were acquired at 3 min intervals, an X-ray incident angle of 0.15° and a 3 s exposure time. For the in-situ light-illuminated device measurements, we used the same set-up as for the GIWAXS measurements of crystals but connected a Keithley 2400 multimeter to the device through a feedthrough. The GIWAXS patterns and current–voltage responses were acquired at 1–2 min intervals, at an X-ray incident angle of 0.24° and a 5 s exposure time.

Temperature-dependent GIWAXS measurements were obtained at both the APS and NSLS-II beamlines. At the APS beamline, temperature-dependent measurements were obtained by cooling to liquid nitrogen temperatures and heating to 80 °C using the Linkam GIXS stage. An incident angle of 0.15° and a 5 s exposure time were used at both beamlines for the temperature measurements.

Three types of sample were used for the in-situ light-illumination measurements: synthesized powder crystals, millimetre-sized single crystals and thin-film devices. Powder crystals were used for the temperature-dependent measurements. Samples were all sealed in an airtight vacuum bag purged with argon right up until the measurement time. Powder GIWAXS measurements were performed by crushing and smearing the powder crystal onto clean glass substrates (wiped with acetone and isopropyl alcohol using Kimwipes).

GIWAXS data processing. GIWAXS data from the APS beamline were processed using the GIXSGUI package (version 1.7.3) running on Matlab 2018b (Mathworks)[46]. GIWAXS data from the NSLS-II beamline were processed using SciAnalysis (https://github.com/CFN-softbio/SciAnalysis) running on Visual Studio Code using Python (v.3.7.3)[47]. All patterns were corrected with conditions such as detector sensitivity, X-ray polarization and geometrical solid-angle parameters.

GIWAXS analysis. To analyse the in-situ light-illuminated GIWAXS measurements, numerical fitting of the diffraction profiles was performed in Matlab 2018b. Each diffraction peak range was fitted with pseudo-Voigt profiles[48]. Each fit used the built-in 'fmincon' function, which constrained the pseudo-Voigt profile to physical ranges in terms of peak line-width (full-width at half-maximum, FWHM). This allowed the fit to discard unphysical domain boundaries and crystallite sizes. Due to the small residual from the 'fmincon' fit, the error interval is smaller than the size of each point in the strain and lattice parameter plot.

The Debye–Scherrer formula was used to extract the average grain size (D_{hkl}) of the 2D perovskites[49]. The first-order out-of-plane diffraction plane was used for the analysis. The shape factor of 0.9 (*K* value in the Scherrer equation) was used[9]. The Scherrer formula is

$$D_{hkl} = \frac{K\lambda}{\beta_{hkl}\cos(\theta_{hkl})}$$

where θ_{hkl} is the Bragg scattering angle, β_{hkl} is the FWHM and λ is the X-ray wavelength. Since this is a grazing scattering geometry with area detectors, we have corrected the FWHM for the beam divergence (β_{div}) and the energy bandwidth (β_{BW})[50]. $\beta_{experiment}$ is the experimentally measured FWHM. The geometric smearing is neglected for small Bragg scattering angles. The FWHM correction is given by

$$\beta_{hkl} = \sqrt{\beta^2_{experiment} - \beta^2_{res}}$$

$$\beta_{res} = \sqrt{\beta^2_{div} + \beta^2_{BW}}$$

Effective interlayer distance calculations. Due to the uniform stacking of the DJ perovskite, the out-of-plane and in-plane diffraction axes are deconvoluted. With this and the assumption that a perovskite octahedra does not undergo a large distortion (confirmed by DFT calculations), we formulate the effective interlayer distance as the following:

$$\text{Effective interlayer distance } (t) = D_{300}\,(t) - 3 \times D_{011}\,(t)$$

where t is the light illumination time, D_{300} is the out-of-plane d spacing (lattice spacing) and D_{011} is the in-plane d spacing.

XPS. XPS measurements were carried out on a PHI Quantera XPS system. Before and after light illumination, XPS was performed on large millimetre-size DJ and RP $n=3$ single-crystal perovskites and films grown on a glass substrate using the procedure mentioned in the first section of the Methods. Etching was not performed, and the sample environment was at 10^{-8} torr for the duration of the experiment. Each peak was averaged using 20–25 collected spectra. Emission spectra were calibrated to carbon 1*s* photoelectron emission at 284.80 eV. The samples were illuminated using an ABB Solar Simulator from Newport (model 94011) for one hour. The XPS spectra were fitted to a pseudo-Voigt profile, and the error was extracted using the 'nlparci' function in MATLAB from the Jacobian of the fit.

Transport characterization. We fabricated an electron-only device with ITO/SnO_2 on one side and then C_{60}/Cu on the other side. The 2D perovskite thin films were measured to be about 250 nm in thickness. The samples were illuminated using an ABB Solar Simulator from Newport (model 94011) for 40 min. The arc simulator modelled AM 1.5G irradiance of 100 mW cm^{-2} and was calibrated using a NIST-certified Si solar cell (Newport 91150V, ISO 17025). The current was measured with a Keithley 2401 instrument at a scan rate of 0.5 V s^{-1}. The device was measured in vacuum (10^{-2} torr). The analysis was performed by fitting in MATLAB and using the optimization package and a numerical least square algorithm 'lsqcurvefit'. An error bar for conductivity and mobility was extracted by using the Jacobian of each time fit. We used the 'nlparci' function in MATLAB's optimization package to extract a 95% confidence interval, and the error was the absolute difference of the interval.

Theoretical structural simulation. *DFT simulations.* The calculations were performed using DFT[51,52] as implemented in the SIESTA package with a basis set of finite-range numerical atomic orbitals[53]. We used the van der Waals density functional with C09 exchange within the van der Waals DF2 flavour to describe the exchange–correlation term[54,55]. This tuning was suggested to improve C09-based geometry optimization over that with DF1 flavour[55]. The latter has already provided a good description of experimental lattice constants similar to those obtained with the optimized generalized-gradient-approximation-based PBEsol functional in solids[56,57]. Norm-conserving Troullier–Martins pseudopotentials were used for each atomic species to account for the core electrons[58]. The $1s^1$; $2s^22p^2$; $2s^22p^3$; $5s^25p^5$ and $5d^{10}6s^26p^2$; and $2s^22p^4$ and $4s^23d^8$ were used as valence electrons for H, C, N, I and Pb, respectively. Polarized double-zeta basis sets with an energy shift of 200 meV were used for the calculations. For the real space mesh grids, an energy cut-off of 600 Rydberg was used. We used the following Monkhorst–Pack k-point grids for the different systems: $2\times8\times8$ for the DJ compound; $4\times1\times4$ and $4\times4\times1$ for the ACI $n=2$ and $n=3$ compounds, respectively; and $6\times1\times6$ for the BA compound. The different structures were fully relaxed using the fast-inertial relaxation engine (FIRE) algorithm, and the maximum force was set to 0.05 eV Å^{-1} (ref. [59]). Since it is not possible in the official distribution of SIESTA to perform structural relaxations while keeping the original symmetries, we constrained the angles of the different structures to 90° (lattice angles $\alpha=\beta=\gamma=90°$) during the geometry optimization such that they remain in their orthorhombic starting systems. Charges were injected into the system by either adding (electron injection) or removing (hole injection) the desired number of electrons. In doing so, the simulation code applies a compensating background charge to maintain the overall neutrality of the system. The procedure that we used to set a net equivalent charge for comparison between the different systems is discussed below.

Modelling net equivalent charges. Due to the considerable difference in the unit cell volume for the different 2D perovskite phases, a common guideline of scaling the net equivalent charges was used to induce the general effect of charge injection. An example of this discrepancy in unit cell volume is that the experimental structure of the DJ compound presents six inorganic $[PbI_6]^{4-}$ octahedra with a volume of 1,810.82 Å^3 while the experimental structure of the RP compound presents 12 $[PbI_6]^{4-}$ octahedra with a volume of 3,987.67 Å^3. Hence, injecting one electron into the DJ structure is not equivalent to injecting one into the RP structure. We used the number of inorganic octahedra as a guide to fix a net equivalent charge for comparison. For example, injecting one charge in the DJ structure with six octahedra would be equivalent to injecting two charges in the RP structure with 12 octahedra. Supplementary Table 2 summarizes the number of charges used to get the net equivalent charges for the different systems. The DJ compound with six octahedra was used as a reference to get the conversion for the other systems based on the number of inorganic octahedra.

Structural model. The starting structures used in the DFT simulations were obtained from previous X-ray diffraction measurements[18,22,44,45]. In the ACI compounds ($n=2$, 3), the first lattice parameter a is ~6.4 Å, which potentially leads to more spurious periodic image interactions when charges are injected into the system. To minimize the latter effect, the cells were doubled along the a direction for both $n=2$ and 3 of the ACI compounds resulting in the a lattice parameter being about 12.8 Å. Due to the molecular positions in the X-ray diffraction data, which are subject to ambiguity because of their dynamic disorder, especially at room temperature, we rotated every second MA molecule to 180° in each plane of the perovskite layer for the ACI compounds[4]. This was to minimize the net dipole in the system. Similarly, for the DJ compound, we rotated every second 4AMP organic barrier molecule to 180°. The results from the geometry optimization of the different systems are summarized in Supplementary Tables 3–5 and 6. For the DJ compound, the results obtained using the experimentally reported molecular 4AMP orientations are also summarized in Supplementary Table 3b for comparison.

Technical comment. We note that relaxing the DJ $n=3$ structures using the Broyden optimization algorithm as implemented in SIESTA presents issues related to the sticking of the systems in local minima. In the case of hole injection at a charge +2, we noticed that the system got stuck at a local minimum not too far from the convergence criteria. In particular, the in-plane lattice parameter tended to be contracted at charge +2, which is in better agreement with experiment. However, given that the convergence on the forces was not fully satisfied, it could be that the in-plane lattice parameters would exhibit a different behaviour if the criteria were met, as in the case of the FIRE relaxation algorithm that we adopted for this work.

Device simulation. *Optical modelling.* The optical absorption for the perovskite cell was modelled using the full-wave solution of Maxwell's equations. The transfer matrix method was used for the planar cell structure. A 300–1,500 nm wavelength range was used in the calculation. Further details can be found in the Supplementary Information, as the same simulation was used in this study[20].

Self-consistent transport simulation. Electron and hole transportation in the solar cell was simulated by MEIDCI, a commercial device simulator software. For carrier transport equations, the generation term in the continuity equation was calculated from the photo-generated profile, and the recombination term in the continuity equation was calculated for direct as well as for defect-assisted Shockley–Read–Hall recombination. Effects from excitons and hot electrons were not accounted for explicitly.

Electrical field profile. To simulate the electric field distribution in the device, a 200 nm perovskite film thickness was selected. Four quantum wells were used for the simulations. The depletion region width for the layer perovskite was from previous studies[24].

Data availability

The data for this study are available from the authors upon reasonable request.

Code availability

The analysis code for this study is available from the authors upon reasonable request.

References

44. Stoumpos, C. et al. Ruddlesden–Popper hybrid lead iodide perovskite 2D homologous semiconductors. *Chem. Mater.* **28**, 2852–2867 (2016).
45. He, X. Oriented growth of ultrathin single crystals of 2D Ruddlesden–Popper hybrid lead iodide perovskite for high-performance photodetector. *ACS Appl. Mater. Interfaces* **11**, 15905–15912 (2019).
46. Jiang, Z. et al. The dedicated high-resolution grazing-incidence X-ray scattering beamline 8-ID-E at the Advanced Photon Source. *J. Synchrotron Radiat.* **19**, 627–636 (2012).
47. Yager, K. G. et al. SciAnalysis. *GitHub* https://github.com/CFN-softbio/SciAnalysis (2021).
48. Sanchez-Bajo, R. & Cumbrera, F. L. The use of the Pseudo-Voigt function in variance method of X-ray line-broadening analysis. *J. Appl. Crystallogr.* **30**, 427–430 (1997).
49. Patterson, A. L. The Scherrer formula for X-ray particle size determination. *Phys. Rev.* **56**, 978–982 (2019).
50. Smiligies, D.-M. Scherrer grain-size analysis adapted to grazing incidence scattering with area detectors. *J. Appl. Crystallogr.* **42**, 1030–1034 (2009).
51. Hohenberg, P. & Kohn, W. Inhomogeneous electron gas. *Phys. Rev.* **136**, B864–B871 (1964).
52. Kohn, W. & Sham, L. J. Self-consistent equations including exchange and correlation effects. *Phys. Rev.* **140**, A1133–A1138 (1965).
53. Soler, J. M. et al. The SIESTA method for ab initio order-N materials simulation. *J. Phys. Condens. Matter.* **14**, 2745–2779 (2002).

54. Cooper, V. W. Van der Waals density functional: an appropriate exchange functional. *Phys. Rev. B* **81**, 161104 (2010).
55. Hamada, I. & Otani, M. Comparative van der Waals density functional study of graphene on metal surfaces. *Phys. Rev. B* **82**, 153412 (2010).
56. Yuk, S. F. et al. Towards an accurate description of perovskite ferroelectrics: exchange and correlations effects. *Sci. Rep.* **7**, 1738 (2017).
57. Traore, B. et al. Importance of vacancies and doping in hole-transporting nickel oxide interface with halide perovskites. *ACS Appl. Mater. Interface* **12**, 6633–6640 (2020).
58. Troullier, N. & Martins, J. L. Efficient pseudopotentials for plane-wave calculations. *Phys. Rev. B* **43**, 1993–2006 (1991).
59. Bitzek, E. et al. Structural relaxation made simple. *Phys. Rev. Lett.* **97**, 170201 (2006).

Acknowledgements

The work at Rice University was supported by the US Department of Defense Short-Term Innovative Research (STIR) programme funded by the Army Research Office. J. Even acknowledges the financial support from the Institut Universitaire de France. W.L. acknowledges the National Science Foundation Graduate Research Fellowship Program. This material is based upon work supported by the National Science Foundation Graduate Research Fellowship Program under grant no. NSF 20-587. Any opinions, findings and conclusions or recommendations expressed in this material are those of the author and do not necessarily reflect the views of the National Science Foundation. Work at Northwestern on the stability of perovskite solar cells was supported by the Office of Naval Research (N00014-20-1-2725). DFT calculations were performed at Institut FOTON as well as Institut des Sciences Chimiques de Rennes, and the work was granted access to the HPC resources of Très Grand Centre de Calcul du CEA (TGCC), the Centre Informatique National de l'Enseignement Supérieur (CINES) and Institut du développement et des ressources en informatique scientifique (IDRIS) under allocations 2019-A0060906724 and 2019-A0070907682 made by Grand Équipement National de Calcul Intensif (GENCI). This research used facilities of the APS, a US Department of Energy Office of Science User Facility operated for the Department of Energy Office of Science by Argonne National Laboratory under contract no. DE−AC02-06CH11357. This research used beamline 11-BM (CMS) of the NSLS-II and the Center for Functional Nanomaterials, both of which are US Department of Energy Office of Science User Facilities operated for the Department of Energy Office of Science by Brookhaven National Laboratory under contract no. DE-SC0012704. We acknowledge the help of B. Chen for supervising the XPS measurements. We thank R. Li for his assistance performing experiments at beamline CMS. The work at Purdue University was supported by the National Science Foundation under grant no. 1724728, CIF21 DIBBs: EI: Creating a Digital Environment for Enabling Data-Driven Science (DEEDS), awarded by the Office of Advanced Cyberinfrastructure.

Author contributions

A.D.M. and J.-C.B. conceived the concept, designed the experiment and wrote the manuscript. S.S. and J. Hoffman synthesized the perovskite crystals and prepared the samples with the help of J. Hou and W.L., and under the supervision of M.G.K.; S.S. fabricated thin films and the solar cells and performed solar cell characterization. W.L. measured and analysed the GIWAXS patterns with the help of H.Z., Y.W., A.F., J. Essman, J.S. and E.T., and performed indexing with guidance from J. Even and J.-C.B. DFT calculations were performed by B.T. with guidance from J. Even and C.K. Device modelling was done by R.A. and advised by M.A.A. J.J.C. helped with the data analysis. All authors read the manuscript and agree to its contents, and all data are reported in the main text and Supplementary Information.

Competing interests

The authors declare no competing interests.

Additional information

Supplementary information The online version contains supplementary material available at https://doi.org/10.1038/s41565-021-01010-2.

Correspondence and requests for materials should be addressed to Jean-Christophe Blancon or Aditya D. Mohite.

Peer review information *Nature Nanotechnology* thanks Diego Solis-Ibarra and the other, anonymous, reviewer(s) for their contribution to the peer review of this work.